The International Journal of Advanced Manufacturing Technology (2019) 100:541–552
https://doi.org/10.1007/s00170-018-2719-x

ORIGINAL ARTICLE

A force model in single grain grinding of long fiber reinforced woven composite

Jinhua Wei[1] · Haoji Wang[1] · Bin Lin[1,2] · Tianyi Sui[1] · Feifei Zhao[1] · Sheng Fang[2]

Received: 9 July 2018 / Accepted: 17 September 2018 / Published online: 26 September 2018

Abstract

The grinding process of long fiber reinforced woven composite (LFRWC) is complicated due to the special structure of the material. The force model is beneficial to understand, predict, and even control the machining process. In this study, a new force model considering fiber orientation of LFRWC is developed based on energy balancing theory. Through the construction of a mathematical model, the study demonstrates the correlation of grinding force with the processing parameters and the composite fiber orientation. A semi-analytical force model based on the specific energy is obtained combining with single grain grinding experiment of 3D orthogonal SiO_2/SiO_2. The influences of grinding parameters on the grinding force are discussed and the major material removal mode is researched. The results show that the predictable model has good consistency with the experimental results, and fiber orientation has a major influence on grinding force. This research on one hand can be used to predict the grinding force of LFRWC, thus conducting the machining and controlling their processing quality; on the other hand, it provides a baseline for selecting the proper machine and tool for LFRWC processing.

Keywords Long fiber reinforced woven composites · Single grain grinding force model · Fiber orientation · Removal mechanism

Nomenclature

R_s	Grinding wheel radius (mm)
h	Height grain cutting into workpiece (mm)
$s(t)$	Cross-section area of grain cutting into workpiece (mm^2)
θ	Half of grain vertex angle (°)
ψ	Angle between grain vertex and vertical direction (rad)
V_ψ	Workpiece displacement when wheel turned ψ (mm)
V_0	Workpiece displacement when the wheel turned 2π (mm)
t_1	The moment grit reaches point B in the first time (s)
l	Contact arc length (mm)
u'	Specific grinding energy proposed (J/mm^3)
F_t	Tangential grinding force (N)
E_{per1}	Energy removing unit volume perpendicular to fiber bundle side surface on direction 1 (J)
E_{par}	Energy removing unit volume parallel to fiber bundle side surface on direction 2 (J)
γ	Volume ratio of parallel to fiber bundle side surface on direction 2
θ'	The angle between F_y and F_n
V_{end}	Removal volume of perpendicular to fiber bundle end surface on direction 1 (mm^3)
V_{par}	Removal volume of parallel to fiber bundle side surface on direction 2 (mm^3)
μ	Friction coefficient among grinding grain, processed material and debris

✉ Bin Lin
tdlinbin@126.com

Jinhua Wei
15222527210@163.com

Haoji Wang
18822408206@163.com

Tianyi Sui
tdsuity@163.com

Feifei Zhao
zhaofeifei760521@163.com

Sheng Fang
fangsheng0666@163.com

[1] Key Laboratory of Advanced Ceramics and Machining Technology, Ministry of Education, Tianjin University, Tianjin, China

[2] Key Laboratory of Advanced Functional Composites, CASC, Beijing, China

F_x	Horizontal force on x-direction
A_1, A_2	Constant coefficient
β_1, β_2	Fitting coefficient of v_s
u_f	Specific energy related to grinding direction
v_s	Grinding wheel speed (mm/s)
v_w	Workpiece feed rate (mm/s)
a_p	Grinding depth (mm)
t_{nmax}	Moment grit cuts out of workpiece (s)
n	Number of grits cut out of workpiece
E	Total work a single grit does in one cut (J)
t_{0max}	The moment grit cuts out of workpiece for the first time (s)
t_{1max}	The moment grit cuts out of workpiece for the second time (s)
t_2	The moment grit reaches point B in the second time (s)
V	Removal volume for one grit (mm^3)
u	General specific grinding energy (J/mm^3)
F_n	Normal grinding force (N)
E_{end}	Energy removing unit volume perpendicular to fiber bundle end surface on direction 1 (J)
E_{per2}	Energy removing unit volume perpendicular to fiber bundle side surface on direction 2 (J)
β	Volume ratio of fiber bundle end surface on direction 1
b	Width grit cutting into workpiece (mm)
V_{per1}	Removal volume of perpendicular to fiber bundle side surface on direction 1 (mm^3)
V_{per2}	Removal volume of perpendicular to fiber bundle side surface on direction 2 (mm^3)
C_F	A constant related to the grinding process
F_y	Vertical force on y-direction
α_1, α_2	Fitting coefficient of a_p
γ_1, γ_2	Fitting coefficient of v_w
R	Safety coefficient

1 Introduction

LFRWC has been widely applied in aerospace, military, and civil areas as it has high fracture toughness, high strength and modulus, good heat-resistant property, and excellent wear-resistant performance [1–4]. However, obvious anisotropy and inhomogeneity as well as processing damages like debonding between fiber and matrix, fiber fracture, and matrix crack make obtaining high-quality surface difficult thus resulting in LFRWC part failure. Therefore, grinding is a main machining approach guaranteeing its quality. Materials are removed through interactions between the grains and workpiece [5], and the grinding process is influenced by grinding parameters including wheel speed, workpiece feed rate and grinding depth, tool geometry, and machined material property [6–8]. Grinding force is one of the most important indicators to study the influence of the machining parameters on the processing [9]. It originated from elastic and plastic deformations of the workpiece, as well as interactions among grains, material, and debris [10, 11]. It is almost related to all grinding factors and is fundamental for researching the grinding process, designing the appropriate tool, and selecting the proper machine. It is also a crucial indicator to evaluate material machining characteristics. Therefore, establishing a corresponding force model related to material properties and grinding parameters is vital to investigate the grinding mechanism and predict the grinding process of LFRWC [12].

So far, researches on machining force of ceramic material both on experimental and analytical aspects have been in-depth and thorough [5, 13–17]. But for LFRWC, because of its complicated structure and various components, the corresponding theory is superficial, and the grinding force model is so different from that of ceramic and metal for the material's anisotropy that a lot of effort still need to be made to establish the model. So far, one of the main focuses is on ultrasonic-assisted machining of LFRWC and the corresponding force model to improve processing quality [18–25]. But the efficiency is lower and more costly than ordinary machining methods'. Though the machining force model of ordinary milling [26], drilling [27], and even grinding [28–30] of LFRWC has also been researched, the theory is always based on fracture mechanics, the maximum undeformed chip thickness, or aggregate force including plowing, scratching, and removing neglecting fiber orientation and idealizing the model because of the complication of woven structure and reinforced particles or short fibers.

In review of the previous work, though LFRWC grinding force has been paid great attention and many experimental studies have already been made, the model considering fiber orientation is a gap. Hence, a grinding force model for LFRWC involving fiber orientation is essential. The present study fills the gap and develops a grinding force model of LFRWC considering fiber orientation based on the energy balancing theory. A semi-analytical force model is obtained combining with 3D orthogonal quartz fiber-reinforced silicon dioxide ceramic matrix (SiO_2/SiO_2) composite single grain grinding experiment. The influence of grinding parameters on specific energy and grinding force is analyzed and the major material removal mechanism is researched. The predictable model is verified. This research on one hand can be used to predict the grinding force of LFRWC thus conducting the machining and controlling their processing quality; on the other hand, it provides a baseline for selecting proper machine and tool for LFRWC processing.

2 Mathematical modeling

Figure 1 shows the grain movement during the grinding process. Points A and C are the locations grit cuts in and out of

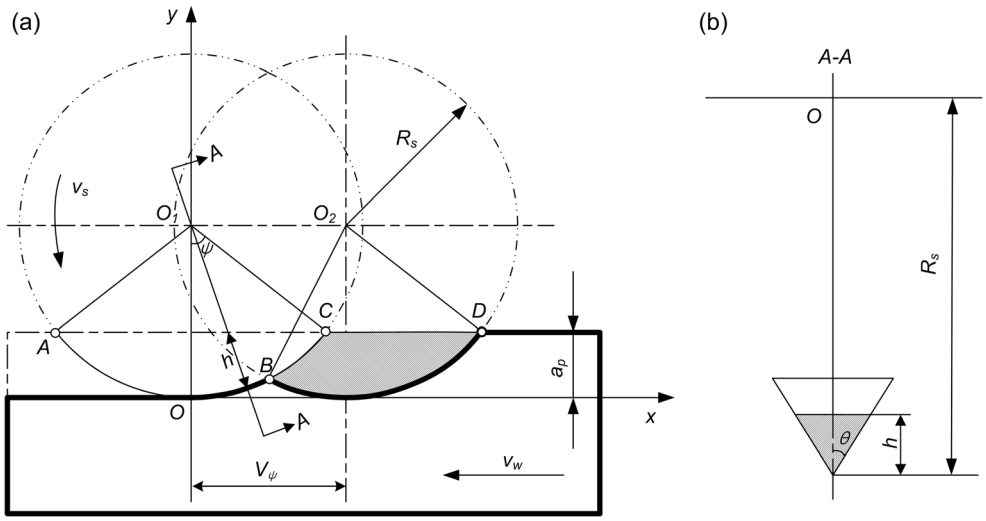

Fig. 1 Sketch of grain movement during grinding process. **a** Grain relative motion track. **b** Cross section of grain cutting into workpiece

workpiece the first time respectively. Points B and D are the places the second time grain contacts and leaves workpiece separately. What should be noted is point B is the coincident point of grit motion track in the first and the second cutting. Therefore, the removal volume is the shaded area BCD for each cut in the following grinding process except for the first one (Fig. 1a). Here, the model is idealized in which the first cut's difference is neglected and it is assumed that the material is completely removed in each cut.

2.1 Grit relative motion track equation

As demonstrated in Fig. 1a, in the XOY coordinate system, grit relative motion track equation is

$$x = R_s\sin\psi + V_\psi \tag{1}$$

$$y = R_s(1-cos\psi) \tag{2}$$

in which R_s (mm) is the radius of the grinding wheel, ψ (rad) is the angle between grain vertex and vertical direction during the grinding process, and V_ψ (mm) is the workpiece displacement in horizontal direction when the wheel turned at angle ψ.

According to the geometric relationship, it can be obtained that

$$\psi = v_s t/R_s \tag{3}$$

$$V_\psi = \frac{V_o}{2\pi}\psi = \frac{2\pi R_s v_w}{v_s}\cdot\frac{\psi}{2\pi} = \frac{\psi R_s v_w}{v_s} \tag{4}$$

In the equations above, t (s) is the time used when the wheel turned at angle ψ, V_0 (mm) is the workpiece displacement in horizontal direction when the wheel turned 2π, v_s (mm/s) is the grinding wheel speed, and v_w (mm/s) is the feed rate of the workpiece.

Substituting Eqs. (3) and (4) into Eqs. (1) and (2), grit relative motion track equation changing over time is

$$x(t) = R_s\sin(v_s t/R_s) + v_w t \tag{5}$$

$$y(t) = R_s(1-cos(v_s t/R_s)) \tag{6}$$

2.2 Cross-section area of grain cutting into workpiece

During the wheel rotation process, h (mm) is the height grain cutting into workpiece and a_p (mm) is the grinding depth. According to Fig. 1a, it can be obtained as follows:

$$\cos(v_s t/R_s) = \left(R_s-a_p\right)/(R_s-h) \tag{7}$$

So,

$$h = R_s-\left(R_s-a_p\right)/\cos(v_s t/R_s) \tag{8}$$

According to Fig. 1b, cross-section area of grain cutting into workpiece is

$$s(t) = \frac{1}{2}\cdot 2h\tan\theta\cdot h = h^2\tan\theta = \left(R_s-\frac{R_s-a_p}{\cos(v_s t/R_s)}\right)^2\tan\theta$$

Where θ (°) is half of the grain vertex angle.

Because $\psi = v_s t/R_s$ is so small that

$$cos(v_s t/R_s)\approx 1 \tag{9}$$

So,

$$s(t)\approx {a_p}^2\tan\theta \tag{10}$$

2.3 Moments grit cutting into and out of workpiece

When grit cuts out of workpiece, $h = 0$ in Eq. (7), so

$$\cos(v_s t_{nmax}/R_s) = 1-a_p/R_s \tag{11}$$

Where t_{nmax} (s) is the moment grit cuts out of workpiece for each cutting process. Hence,

$$t_{nmax} = \frac{R_s}{v_s}\arccos\left(1-\frac{a_p}{R_s}\right) + 2n\pi\frac{R_s}{v_s}(n = 0, 1, 2, 3.....) \quad (12)$$

In Eq. (12), $n = 0$ shows grit cuts out of workpiece the first time and $n = 1$ is the second time, and so on. That is to say, at point C $n = 0$ and at point D $n = 1$ in Fig. 1a, so

$$t_{0max} = \frac{R_s}{v_s}\arccos\left(1-\frac{a_p}{R_s}\right), \quad t_{1max} = \frac{R_s}{v_s}\arccos\left(1-\frac{a_p}{R_s}\right) + 2\pi\frac{R_s}{v_s} \quad (13)$$

It is assumed that the moment grit reaches point B at adjacent two times is t_1 (s) and t_2 (s), respectively, hence,

$$x(t_1) = x(t_2) y(t_1) = y(t_2)$$

According to Eqs. (5) and (6),

$$R_s\sin(v_s t_1/R_s) + v_w t_1 = R_s\sin(v_s t_2/R_s) + v_w t_2 \quad (14)$$

$$R_s[1-cos(v_s t_1/R_s)] = R_s[1-cos(v_s t_2/R_s)] \quad (15)$$

From Eq. (15), it can be obtained

$$cos(v_s t_1/R_s) = cos(v_s t_2/R_s)$$

Combining grit real motion track and trigonometric function knowledge, it can be seen that

$$v_s t_1/R_s = 2\pi - v_s t_2/R_s$$

So,

$$t_2 = 2\pi R_s/v_s - t_1 \quad (16)$$

From Eq. (14), it can be obtained

$$R_s[\sin(v_s t_1/R_s) - \sin(v_s t_2/R_s)] = v_w(t_2 - t_1) \quad (17)$$

Substituting Eq. (16) into Eq. (17), then

$$\sin(v_s t_1/R_s) = \pi v_w/v_s - v_w t_1/R_s$$

For $\psi = v_s t_1/R_s$ is so small that $\sin(v_s t_1/R_s) \approx v_s t_1/R_s$, then

$$t_1 = \pi\frac{v_w}{v_s}\frac{R_s}{v_s + v_w} \quad (18)$$

Substituting Eq. (18) into Eq. (16), then

$$t_2 = \frac{\pi R_s}{v_s}\left(2-\frac{v_w}{v_s + v_w}\right) \quad (19)$$

To identify which is the moment grit reaches point B the first time, the value of t_1 and t_2 is compared with each other's, then

$$t_2 - t_1 = \frac{2\pi R_s}{v_s}\left(1-\frac{v_w}{v_s + v_w}\right) > 0$$

Therefore, t_1 is the moment grit reaches point B the first time and t_2 is the moment in the second time.

2.4 Contact arc length between the grain and workpiece

The unit contact arc length dl during the grinding process is calculated as follows:

$$dx = (v_s cos(v_s t/R_s) + v_w)dt$$
$$dy = v_s\sin(v_s t/R_s)dt$$
$$dl = \sqrt{dx^2 + dy^2} = \sqrt{v_s^2 + 2v_s v_w cos(v_s t/R_s) + v_w^2}dt$$

Because of Eq. (9), then

$$dl \approx (v_s + v_w)dt \quad (20)$$

Therefore, the contact arc length between the grain and workpiece for one cutting process is

$$l = \int_{t_2}^{t_{1max}} dl = \int_{t_2}^{t_{1max}} (v_s + v_w)dt = \frac{R_s(v_s + v_w)}{v_s}\left[arccos\left(1-\frac{a_p}{R_s}\right) + \frac{\pi v_w}{v_s + v_w}\right] \quad (21)$$

Assuming that $\alpha = arccos\,(1 - a_p/R_s)$, then

$$cos\alpha = 1-a_p/R_s, \sin\alpha = \sqrt{1-\cos^2\alpha} = \sqrt{2a_p/R_s - a_p^2/R_s^2}$$

For $a_p \ll R_s$, so

$$a_p^2/R_s^2 \approx 0, \sin\alpha \approx \alpha$$

That is to say,

$$\alpha \approx \sqrt{2a_p/R_s - a_p^2/R_s^2} \approx \sqrt{2a_p/R_s} \quad (22)$$

Substituting Eq. (22) into Eq. (21), then

$$l = \frac{R_s(v_s + v_w)}{v_s}\left(\sqrt{\frac{2a_p}{R_s}} + \frac{\pi v_w}{v_s + v_w}\right) = \sqrt{2a_p R_s} + \frac{v_w}{v_s}\left(\sqrt{2a_p R_s} + \pi R_s\right) \quad (23)$$

2.5 Removal volume for one cut

Based on Fig. 1a, removal volume for one grit is

$$V = \int_{t_2}^{t_{1max}} s(t)dl - \int_{t_1}^{t_{0max}} s(t)dl = \int_{t_2 + t_{0max}}^{t_1 + t_{1max}} s(t)dl \quad (24)$$

Substituting Eqs. (10), (13), (18), (19), and (20) into Eq. (24), then

$$V = \int_{t_2 + t_{0max}}^{t_1 + t_{1max}} a_p^2\tan\theta(v_s + v_w)dt = 2\pi R_s\tan\theta a_p^2 v_w/v_s \quad (25)$$

2.6 Specific grinding energy model

Specific grinding energy reflects the consumed energy for removing unit volume workpiece material. During one cutting process, the total work single grit does is $E = F_t(v_s + v_w)(t_{1\max} - t_2)$ where F_t is the tangential grinding force and the total removal volume is Vas Eq. (25) shows. Therefore, the specific grinding energy is

$$u' = E/V = \frac{F_t(v_s + v_w)}{2a_p{}^2 v_w \tan\theta} \cdot \frac{arccos\left(1-a_p/R_s\right) + \pi v_w/(v_s + v_w)}{\pi} \quad (26)$$

In general, the general specific grinding energy $u = \frac{F_t(v_s+v_w)}{v_w a_p b}$ in which b is the width grit cutting into the workpiece when grinding depth is a_p for single grain grinding. Here, $b = 2a_p \tan\theta$; so,

$$u = \frac{F_t(v_s + v_w)}{2a_p{}^2 v_w \tan\theta} \quad (27)$$

In Section 4.1, the model we proposed is compared with the general model and its reasonability is explained.

2.7 Grinding force analytical model

Figure 2 shows the relation sketch between fiber orientation of 3D orthogonal LFRWC and grinding direction. There are two fiber orientations on both grinding directions respectively:

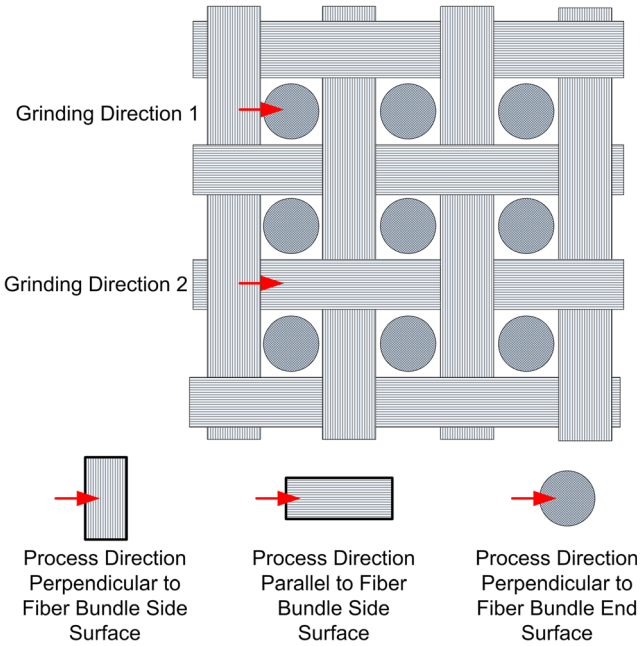

Fig. 2 Relation sketch between fiber orientation of 3D orthogonal LFRWC and grinding direction

perpendicular to fiber bundle end and side surface on direction 1, and perpendicular and parallel to fiber bundle side surface on direction 2.

It is assumed that the required energies removing unit volume perpendicular to fiber bundle end and side surface are respectively E_{end} and E_{per1} on direction 1, that removing unit volumes parallel and perpendicular to fiber bundle side surface are E_{par} and E_{per2}, and the volume ratios of fiber bundle end surface on direction 1 and parallel to fiber bundle side surface on direction 2 are β and γ separately, then

On direction 1:

$$V_{\text{end}} = \beta V, V_{\text{per1}} = (1-\beta)V$$

On direction 2:

$$V_{\text{par}} = \gamma V, V_{\text{per2}} = (1-\gamma)V$$

Where V_{end} and V_{per1} are the removal volumes of perpendicular to fiber bundle end and side surface on direction 1, V_{par} and V_{per2} are the removal volumes of parallel and perpendicular to fiber bundle side surface on direction 2.

So on direction 1, the needed energy removing volume $V$is

$$E_1 = V_{\text{end}}E_{\text{end}} + V_{\text{per1}}E_{\text{per1}} = E_{\text{end}}\beta V + E_{\text{per1}}(1-\beta)V \quad (28)$$

On direction 2, the needed energy removing volume $V$is

$$E_2 = V_{\text{par}}E_{\text{par}} + V_{\text{per2}}E_{\text{per2}} = E_{\text{par}}\gamma V + E_{\text{per2}}(1-\gamma)V \quad (29)$$

According to energy balance in one cut, so

$$E = F_t l \quad (30)$$

Substituting Eqs. (23), (25), (28), and (29) into Eq. (30), then

On direction 1:

$$F_t = E_1/l = \frac{2\pi R_s \tan\theta a_p{}^2 v_w \left[E_{\text{end}}\beta + E_{\text{per1}}(1-\beta)\right]}{\sqrt{2a_p R_s}(v_w + v_s) + \pi R_s v_w} \quad (31)$$

On direction 2:

$$F_t = E_2/l = \frac{2\pi R_s \tan\theta a_p{}^2 v_w \left[E_{\text{par}}\gamma + E_{\text{per2}}(1-\gamma)\right]}{\sqrt{2a_p R_s}(v_w + v_s) + \pi R_s v_w} \quad (32)$$

In the formulas above, E_{end}, E_{per1}, E_{par}, and E_{per2} are all related to processing parameters and material properties of each fiber orientation.

If the composite is not 3D orthogonal, fiber orientation cannot be identified obviously, assuming that $u_f = E_{\text{end}}\beta + E_{\text{per1}}(1-\beta)$ or $u_f = E_{\text{par}}\gamma + E_{\text{per2}}(1-\gamma)$, then

$$F_t = \frac{2\pi R_s \tan\theta a_p{}^2 v_w u_f}{\sqrt{2a_p R_s}(v_w + v_s) + \pi R_s v_w} \quad (33)$$

In which u_f is the specific energy related to grinding direction and fiber orientation.

Then, normal force F_n can be obtained through formula (34) as follows:

$$F_n = (F_t \pm C_F)/\mu \tag{34}$$

Here, μ is the friction coefficient among grinding grain, processed material surface, and debris, and C_F is a constant which is related to the grinding process.

3 Experiment

Grinding experiments are performed on the JDUT400E CNC Machine. The grinding wheel is customized with a single diamond grain and its specific parameters are in Table 1. The real grinding process is shown in Fig. 3. The dynamometer is Kistler 9257A and the data acquisition system is Kistler 5070A. The workpiece used for this investigation is 3D orthogonal SiO_2/SiO_2 which is used in the structural components of aerospace field. The relation between fiber orientation and grinding direction has been reflected in Fig. 2. The specimens have the dimensions of 50 mm × 25 mm × 15 mm and grinding is along the longest direction with the grain engaged across the entire workpiece length. Single-factor experiment is adopted. Experimental condition is reflected in Table 1. What should be highlighted is when one of the grinding parameters changes, the other two are those with parentheses and fixed. Grinding type during the process is up-grinding without coolant and dynamometer sampling frequency is 20 kHz. The ground surfaces are observed using Phenom SEM after experiments.

4 Results and discussion

4.1 Specific grinding energy

During the grinding process, forces in x-direction and y-direction are acquired by a dynamometer, then the tangential force F_t and the normal force F_n are calculated by Eq. (35) as follows:

Table 1 Experimental condition

Types	Content
Grinding wheel radius R_s (mm)	13.6
Grain vertex half angle θ (°)	38.7
Grinding wheel speed v_s (r/min)	1000, 1500, (2000), 2500, 3000
Feed rate of workpiece v_w (mm/min)	(500), 550, 600, 650, 700
Grinding depth a_p (mm)	(0.1), 0.12, 0.14, 0.16, 0.18

$$F_n = F_x \sin\theta' + F_y \cos\theta'; \quad F_t = F_x \cos\theta' - F_y \sin\theta' \tag{35}$$

Where $\theta' = 2/3 \arccos(1 - a_p/R_s)$, it is the included angle between the vertical force F_y on the y-direction and the normal force F_n acting on the grinding zone [14]. F_x is the horizontal force on the x-direction. Through Eqs. (26) and (27), the specific grinding energies of our proposed model and the general model are obtained. Their changing trends with different grinding parameters are shown in Fig. 4. It shows that the specific grinding energy sharply decreases with increasing wheel speed and increases slightly with the increasing feed rate and grinding depth on both processing directions. Specific energy of direction 1 is larger than that of direction 2 under the same processing parameters. The proposed specific energies and the general ones have the same changing trends with each other under grinding parameters, but the values and the order of magnitude have an enormous difference. Why is there such a big variance?

The general specific energy model is obtained on a macroscopic scale which thinks that all grains on the wheel are taking part in the grinding process and they have no period without contact with the workpiece. So, the removal volume of unit time is an expected value. But on a microscopic scale, the real situation is different. Not all grains participate in the process and some of them may not come in contact with the workpiece during one cut because the heights of the grain edge are different relative to workpiece under some depth. Therefore, even in the conventional wheel grinding process, the specific energy calculated according to the general model is bigger than the real value. So, the general specific energy is just an expected value.

There are two main factors resulting in the difference between the general and the proposed models. In the proposed model, the specific energy is deduced on a microscopic scale. One main factor is the model in our research is based on single grain which is always taking part in the machining in each cut. The grain edge height is constant relative to the workpiece when the grinding depth is fixed. The other main factor is the model considers the contact period from t_2 to $t_{1\max}$ between the grain and workpiece in one cut as Section 2.3 discussed. It can be obviously known that from the moment $t_{1\max}$ to the next time grain cutting into workpiece, single grain no longer has contact with material and does not take part in grinding anymore. Therefore, the angle ratio comparing Eqs. (26) and (27) appears and the specific energy is smaller.

In fact, for each grain taking part in grinding, it does not always have contact with the workpiece during conventional wheel grinding, but when it cuts out of workpiece or is within cutting process, there are other grains participating in cutting. Therefore, for conventional wheel grinding, the process is successive on a macroscopic scale; but for single grinding, the process is discontinuous no matter on a macroscopic or microscopic scale.

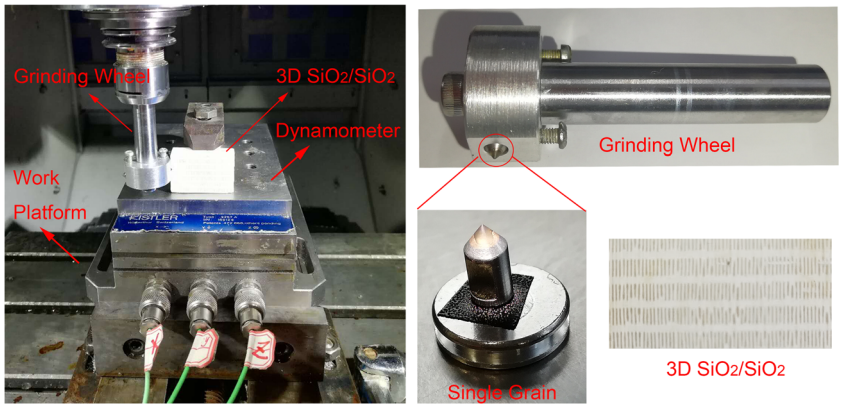

Fig. 3 Grinding experiment setup

4.2 Grinding force semi-analytical force model

Because it is difficult to obtain the required energy removing unit volume of each fiber orientation, a whole specific energy related to grinding parameters and fiber orientations on each grinding direction is assumed. Therefore,

$$E_{\mathrm{end}}\beta + E_{\mathrm{per1}}(1-\beta) = u_1{}' = A_1 a_p{}^{\alpha_1}(v_s/10,000)^{\beta_1}(v_w/10)^{\gamma_1} \quad (36)$$

$$E_{\mathrm{par}}\gamma + E_{\mathrm{per2}}(1-\gamma) = u_2{}' = A_2 a_p{}^{\alpha_2}(v_s/10,000)^{\beta_2}(v_w/10)^{\gamma_2} \quad (37)$$

In Eqs. (36) and (37), A_1, A_2, α_1, α_2, β_1, β_2, γ_1, and γ_2 are the fitting coefficients which are related with fiber orientation; the units of a_p, v_s, and v_w are millimeter, millimeters per second, and millimeter per seconds. The constant coefficient 10,000 of v_s and 10 of v_w is to adjust the order of magnitude. The conversion relationships of different units v_s and v_w are shown as follows:

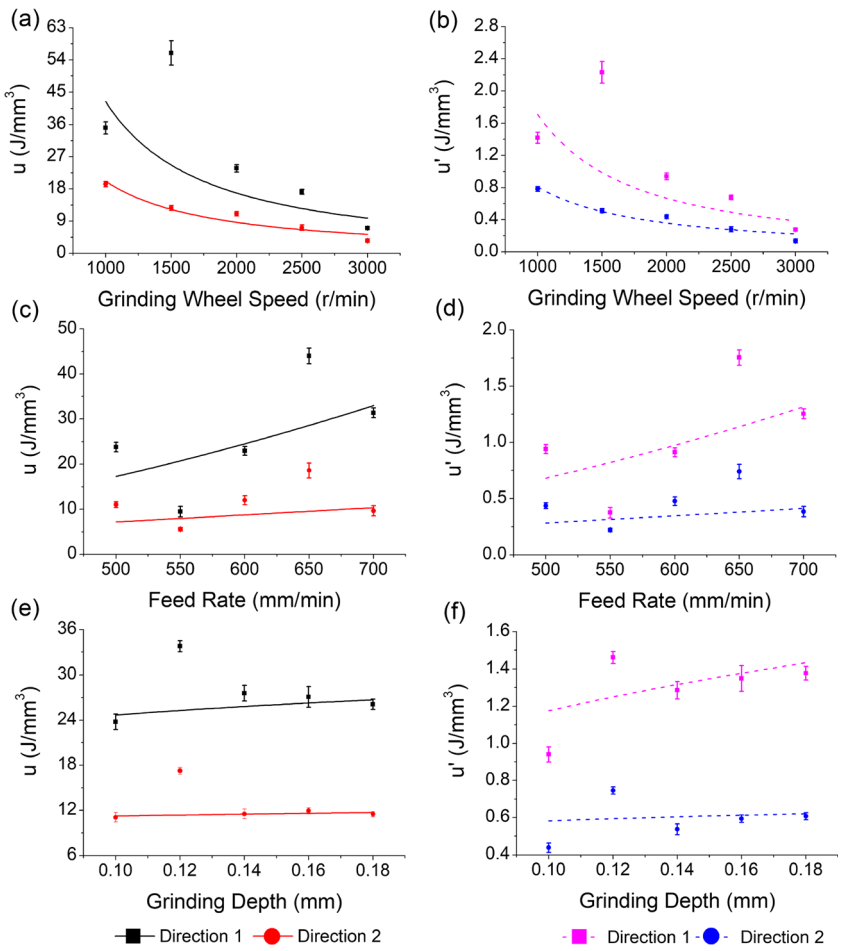

Fig. 4 Trends of specific grinding energy with different grinding parameters. **a**, **c**, **e** General specific energy. **b**, **d**, **f** Proposed specific energy

$$v_s(\mathrm{mm/s}) = 2\pi R_s v_s(r/min)/60 \tag{38}$$

$$v_w(\mathrm{mm/s}) = v_w(mm/min)/60 \tag{39}$$

According to the experimental results, the fitting coefficients are obtained through simulated annealing algorithm.

$$u_1{}' = 3.053{a_p}^{0.769}(v_s/10,000)^{-0.596}(v_w/10)^{0.855} \tag{40}$$

$$u_2{}' = 0.675{a_p}^{0.611}(v_s/10,000)^{-0.841}(v_w/10)^{0.445} \tag{41}$$

The fitting coefficients in Eqs. (40) and (41) are corresponding to the trends of specific energy in Fig. 4b, d, f. Substituting Eqs. (40) and (41) into Eqs. (31) and (32), the semi-analytical tangential force models of both grinding directions are acquired.

$$F_{t1} = \frac{206.4\pi R_s \tan\theta {v_s}^{-0.596}{a_p}^{2.769}{v_w}^{1.855}}{\sqrt{2a_pR_s}(v_w+v_s)+\pi R_s v_w} \tag{42}$$

$$F_{t2} = \frac{1120.3\pi R_s \tan\theta {v_s}^{-0.841}{a_p}^{2.611}{v_w}^{0.445}}{\sqrt{2a_pR_s}(v_w+v_s)+\pi R_s v_w} \tag{43}$$

Figure 5 is the grinding force ratio of different processing parameters on both directions. Through linear fitting, the relation between F_n and F_t is obtained as Eqs. (44), (45), and (46) show. Then, the semi-analytical normal force models can be calculated through Eqs. (42) and (43).

When the grinding wheel speed changes:

$$\begin{Bmatrix} F_{n1} \\ F_{n2} \end{Bmatrix} = \begin{Bmatrix} (F_{t1}+0.090)/0.685 \\ (F_{t2}+0.354)/0.834 \end{Bmatrix} \tag{44}$$

When the feed rate changes:

$$\begin{Bmatrix} F_{n1} \\ F_{n2} \end{Bmatrix} = \begin{Bmatrix} (F_{t1}-0.204)/0.387 \\ (F_{t2}-0.032)/0.431 \end{Bmatrix} \tag{45}$$

When the grinding depth changes:

$$\begin{Bmatrix} F_{n1} \\ F_{n2} \end{Bmatrix} = \begin{Bmatrix} (F_{t1}-0.597)/0.340 \\ (F_{t2}-0.121)/0.390 \end{Bmatrix} \tag{46}$$

It can be known from Fig. 5 that the friction coefficient between tool and workpiece of direction 1 is smaller than that of direction 2 during grinding. Figure 6 shows the SEM images of ground surface on both directions. It reflects that on direction 1, material removal modes are simple: fiber side surface is sheared off with smooth fracture, fiber end surface is cut off (Fig. 6a), and plastic deformation occurs on matrix around grain apex (Fig. 6b). The contact zone between the grain and workpiece has no remaining debris; while on direction 2, the removal modes are varied: parallel to fiber bundle side surface is broken (Fig. 6c) or fractured debonding from matrix (Fig. 6d), perpendicular to fiber bundle side surface is sheared off with irregular fracture (Fig. 6e), matrix is cracked (Fig. 6f), but there are quantities of debris including fractured fibers and cracked matrix leaving the contact zone. The remaining debris and irregular fracture will increase the friction interaction between the grain and workpiece. Therefore, the friction coefficient of direction 1 is smaller than that of direction 2. The removal mechanism is brittle fracture of fiber and matrix except for partial matrix plastic deformation around cutting edge.

4.3 Force model verification

Figure 7 shows the experimental and fitting results of grinding force with changing processing parameters. The fitting results are in good accordance with the experimental ones, which reflects the force model is reasonable. Meanwhile, grinding force has the similar trend with specific energy (Fig. 4), while the processing parameters change. That is because a larger wheel speed will reduce the plastic deformation and increase brittle fracture of the material, thus causing the grinding process to be steadier, the specific energy and the grinding force to decrease.

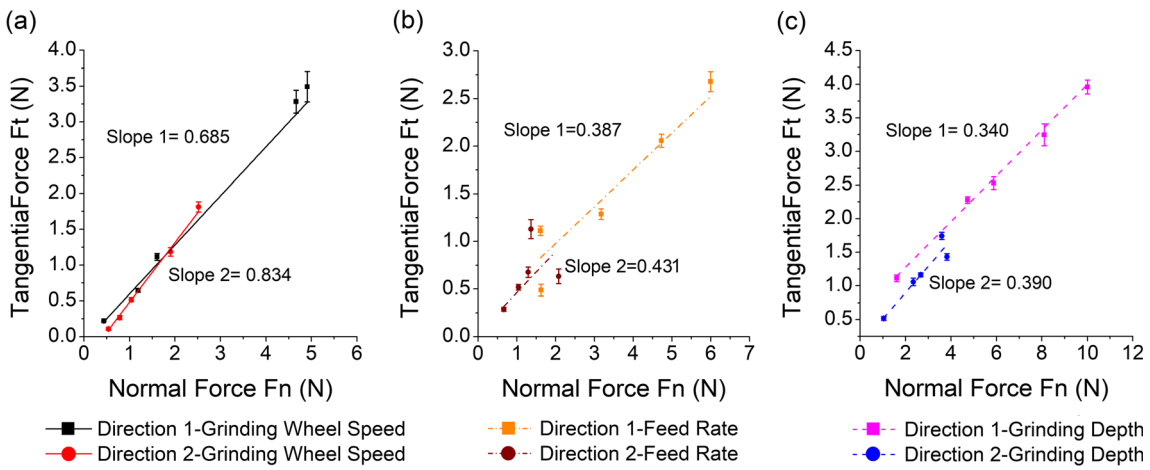

Fig. 5 Grinding force ratio of different processing parameters. **a** Under changing wheel speed. **b** Under changing feed rate. **c** Under changing grinding depth

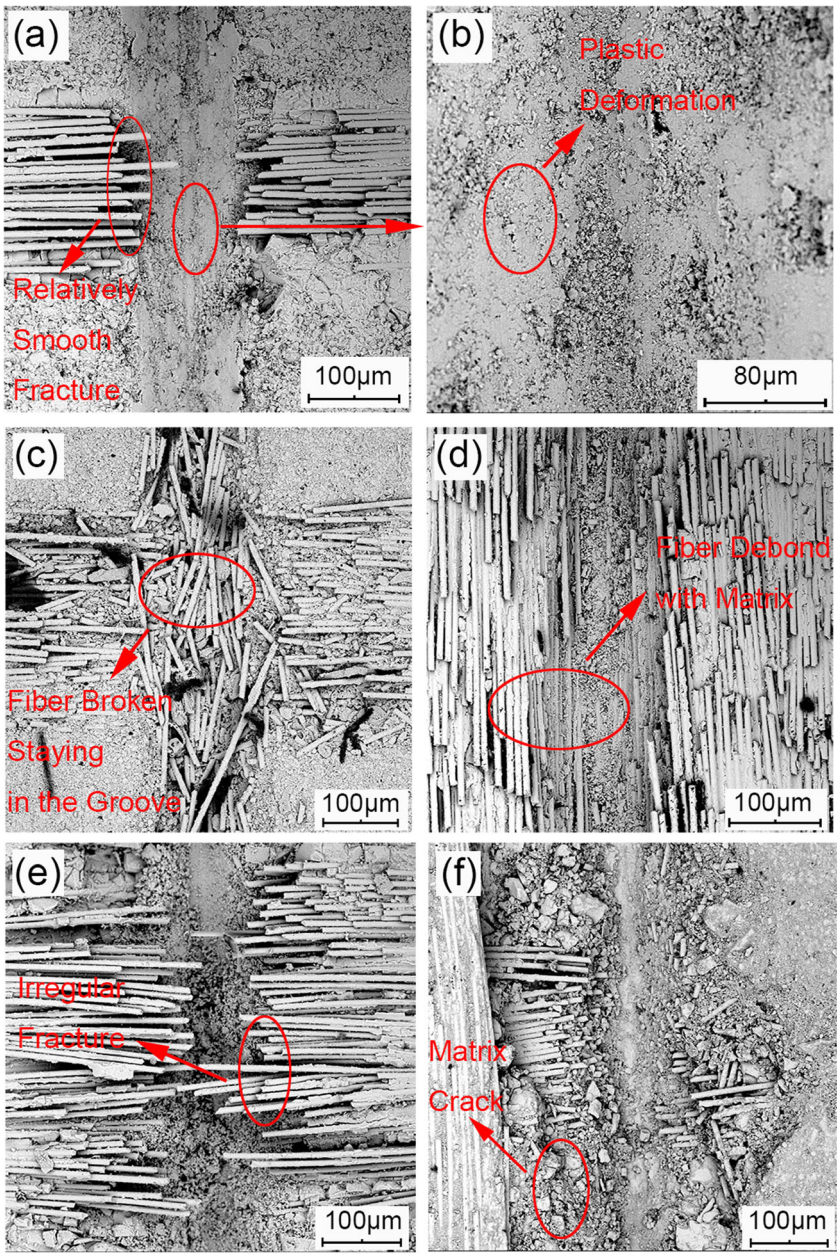

Fig. 6 SEM images of ground surface. **a**, **b** Grinding direction 1. **c**, **d**, **e**, **f** Grinding direction 2

Increasing feed rate, inversely, reduces the brittle fracture and increases the plastic deformation of the material resulting in a larger specific energy and grinding force. Larger grinding depth means cutting more layers of fiber at one time. Therefore, the integrated effects make the specific energy and the grinding force increase. From the global, the force and the specific energy are not just going up or down, there are some fluctuations with the grinding parameters. The main reason is that the presence of reinforced fibers causes their fluctuations [30].

4.4 Maximum grinding force during processing

During the grinding process, average force is the stable output response of material to the machine input, while the maximum force is the instant output response, so it has a huge destruction to the processing machine and the tool. Therefore, the maximum force during processing is the test of the impact resistance of the machine and the tool and is also the fundamental standard for their selection. In our experiment, the maximum ratio between the maximum and average force is 2.79, so assuming the safety coefficient R is 3, then the analytical model of the maximum force is obtained by Eqs. (31) and (32) multiplying safety coefficient R.

Figure 8 shows the changing trends of maximum grinding force with different processing parameters. It also has the same tendency with the average force and the specific energy. The normal forces are always bigger than the tangential ones on both directions. That is because SiO_2 fiber is a hard and

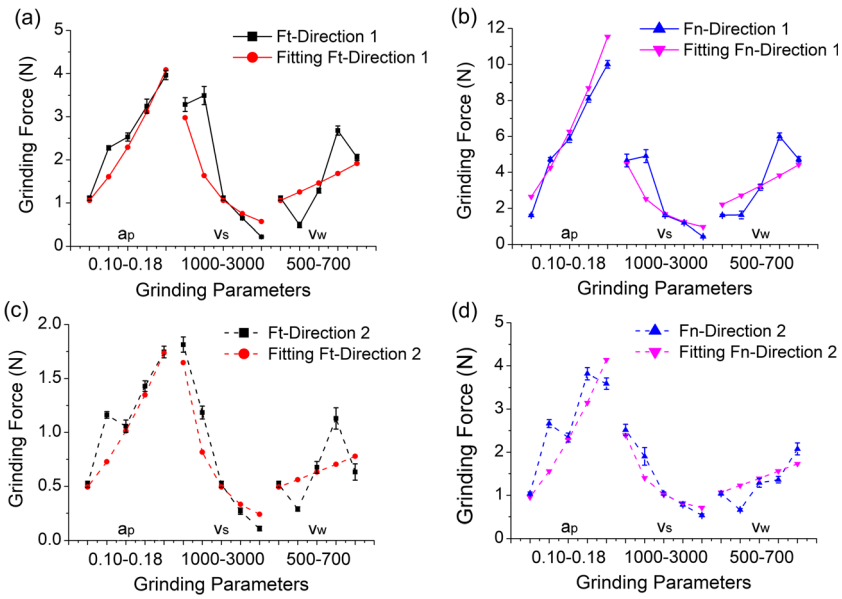

Fig. 7 Comparison between experimental and fitting results. **a** F_t on direction 1. **b** F_n on direction 1. **c** F_t on direction 2. **d** F_n on direction 2

brittle material; during the grinding process, it is more difficult for grain edge cutting into workpiece than moving along it. Therefore, the normal force is larger than the tangential one.

Another fact is that the specific energy (Fig. 4), average force (Fig. 7), and maximum force (Fig. 8) of direction 1 are always larger than those of direction 2 under the same

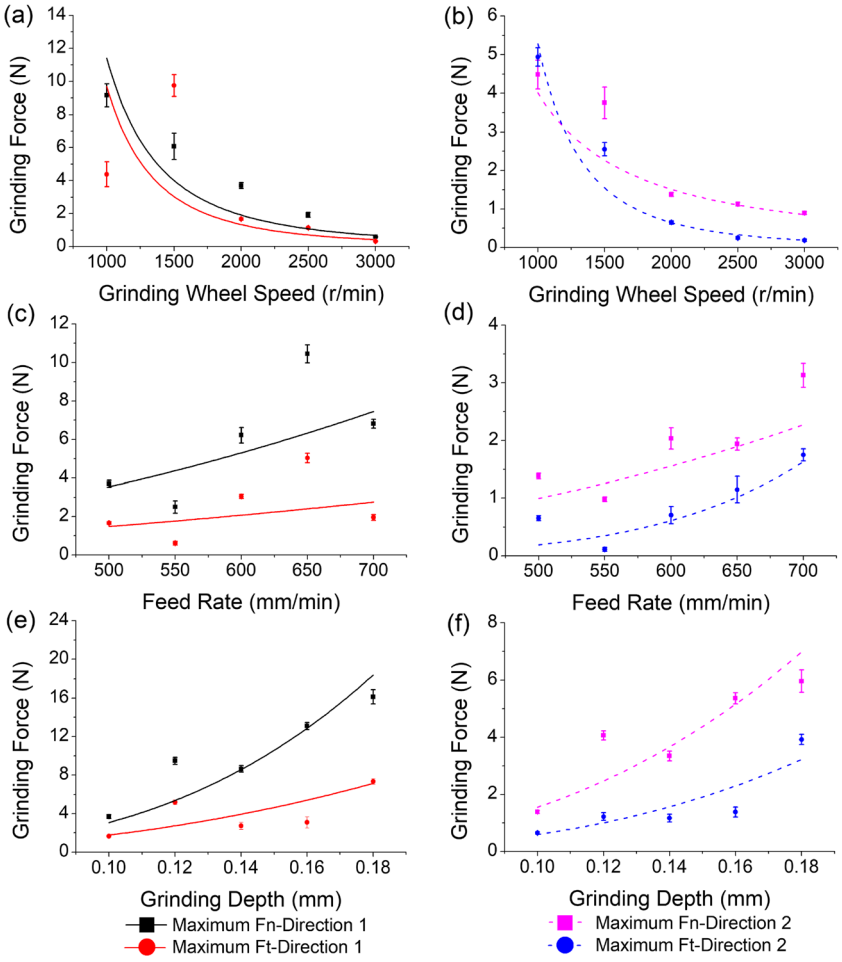

Fig. 8 Maximum grinding force with different processing parameters. **a**, **c**, **e** Direction 1. **b**, **d**, **f** Direction 2

grinding parameters. The reason is on direction 1, removing material should cut off fiber end surface and shear off fiber side surface. While on direction 2, perpendicular to fiber side surface is sheared off and meanwhile there is no fiber bundle end surface playing a fixing role at both its sides which leads to irregular cutting fracture, so the needed energy removing them is slightly larger than that for direction 1 because of the friction between grain and fibers with varying lengths; for parallel to fiber bundle side surface, long fibers suffer pressure along its length orientation then break easily because of the unstable principle of compression beam for slender rod, or they debond from matrix owing to the weak interlaminar performance, so the needed energy is much smaller than removing the same volume fiber end surface on direction 1. The integrated energy removing the same volume material on direction 2 is smaller than that for direction 1, so the force is also smaller. Because fiber orientation is different on both processing directions, the removing energy required and the grinding force are varied. Therefore, fiber orientation has a major influence on specific energy and grinding force.

5 Conclusions

In this study, a new force model of LFRWC considering fiber orientation was proposed based on energy balancing theory and verified with the single grain grinding experiment results of 3D orthogonal SiO_2/SiO_2. The main findings are listed as follows:

1. The study modifies the specific grinding energy model and proposes an analytical model to predict LRFWC grinding force in single grain processing in terms of fiber orientation.
2. The study establishes a semi-analytical force model aiming at single grain grinding of 3D orthogonal SiO_2/SiO_2 composite using simulated annealing algorithm. The model is well verified by experiment results and is proved to be viable.
3. The mechanism on how fiber orientation influences specific and grinding force is explained based on experiment results and SEM images combining with friction and pressing staff steady theory.
4. Through the grinding experiments, the grinding force and the specific energy decrease with the increasing wheel speed but increase with the increasing feed speed and grinding depth.
5. The maximum force during the grinding process is the reference standard to choose the machine and the tool. Its theoretical model can be obtained through multiplying the average force model by a safety coefficient.
6. During grinding process, the force and specific energy of direction 1 are always larger than those of direction 2 and the normal force is always bigger than the tangential force.
7. The main removal mode of 3D orthogonal SiO_2/SiO_2 composite during the grinding process is brittle fracture of fiber and matrix except for partial matrix plastic deformation around the cutting edge.

Acknowledgements The authors are grateful for Engineer Shigang Dai's valuable advices on test design during the experiment process, thus making the results have good reliability and repeatability.

Funding Information This study received financial assistance from the National Natural Science Foundation of China (NO.51375333).

References

1. Söderfjäll M, Herbst HM, Larsson R, Almqvist A (2017) Influence on friction from piston ring design, cylinder liner roughness and lubricant properties. Tribol Int. https://doi.org/10.1016/j.triboint.2017.07.015
2. Erol O, Powers BM, Keefe M (2017) Effects of weave architecture and mesoscale material properties on the macroscale mechanical response of advanced woven fabrics. Compos A: Appl Sci Manuf 101:554–566. https://doi.org/10.1016/j.compositesa.2017.07.016
3. Hosseini Monazzah A, Pouraliakbar H, Bagheri R, Seyed Reihani SM (2017) Al-Mg-Si/SiC laminated composites: fabrication, architectural characteristics, toughness, damage tolerance, fracture mechanisms. Compos Part B 125:49–70. https://doi.org/10.1016/j.compositesb.2017.05.055
4. Cao HM, Zhou X, Li XY, Lu K (2017) Friction mechanism in the running-in stage of copper: from plastic deformation to delamination and oxidation. Tribol Int 115:3–7. https://doi.org/10.1016/j.triboint.2017.05.027
5. Malkin S, Hwang TW (1996) Grinding mechanisms for ceramics. CIRP Ann Manuf Technol 45(2):569–580. https://doi.org/10.1016/S0007-8506(07)60511-3
6. Badger JA, Torrance AA (2000) A comparison of two models to predict grinding forces from wheel surface topography. Int J Mach Tools Manuf 40(8):1099–1120. https://doi.org/10.1016/S0890-6955(99)00116-9
7. Xiao X, Zheng K, Liao W, Meng H (2016) Study on cutting force model in ultrasonic vibration assisted side grinding of zirconia ceramics. Int J Mach Tools Manuf 104:58–67. https://doi.org/10.1016/j.ijmachtools.2016.01.004
8. Zhang Z, Huo F, Wu Y, Huang H (2011) Grinding of silicon wafers using an ultrafine diamond wheel of a hybrid bond material. Int J Mach Tools Manuf 51(1):18–24. https://doi.org/10.1016/j.ijmachtools.2010.10.006
9. Ren YH, Zhang B, Zhou ZX (2009) Specific energy in grinding of tungsten carbides of various grain sizes. CIRP Ann 58(1):299–302. https://doi.org/10.1016/j.cirp.2009.03.026
10. Sambhav K, Kumar A, Choudhury SK (2011) Mechanistic force modeling of single point cutting tool in terms of grinding angles. Int J Mach Tools Manuf 51(10):775–786. https://doi.org/10.1016/j.ijmachtools.2011.06.007
11. Sun J, Qin F, Chen P, An T (2016) A predictive model of grinding force in silicon wafer self-rotating grinding. Int J Mach Tools Manuf 109:74–86. https://doi.org/10.1016/j.ijmachtools.2016.07.009

12. Park HW, Liang SY (2008) Force modeling of micro-grinding incorporating crystallographic effects. Int J Mach Tools Manuf 48(15):1658–1667. https://doi.org/10.1016/j.ijmachtools.2008.07.004
13. Zhang Y-N, Lin B, Liu J-J, Song X-F, Key J (2015) An experimental study on mechanical modeling of ceramics based on microstructure. Appl Sci 5(4):1337–1349. https://doi.org/10.3390/app5041337
14. Huang H, Liu YC (2003) Experimental investigations of machining characteristics and removal mechanisms of advanced ceramics in high speed deep grinding. Int J Mach Tools Manuf 43(8):811–823. https://doi.org/10.1016/S0890-6955(03)00050-6
15. Yang M, Li C, Zhang Y, Jia D, Zhang X, Hou Y, Li R, Wang J (2017) Maximum undeformed equivalent chip thickness for ductile-brittle transition of zirconia ceramics under different lubrication conditions. Int J Mach Tools Manuf 122:55–65. https://doi.org/10.1016/j.ijmachtools.2017.06.003
16. Zhang Y, Li C, Ji H, Yang X, Yang M, Jia D, Zhang X, Li R, Wang J (2017) Analysis of grinding mechanics and improved predictive force model based on material-removal and plastic-stacking mechanisms. Int J Mach Tools Manuf 122:81–97. https://doi.org/10.1016/j.ijmachtools.2017.06.002
17. Xi X, Yu T, Ding W, Xu J (2018) Grinding of Ti2AlNb intermetallics using silicon carbide and alumina abrasive wheels: tool surface topology effect on grinding force and ground surface quality. Precis Eng 53:134–145. https://doi.org/10.1016/j.precisioneng.2018.03.007
18. Ding K, Fu Y, Su H, Cui F, Li Q, Lei W, Xu H (2017) Study on surface/subsurface breakage in ultrasonic assisted grinding of C/SiC composites. Int J Adv Manuf Technol 91(9–12):3095–3105. https://doi.org/10.1007/s00170-017-0012-z
19. Ning F, Cong W, Wang H, Hu Y, Hu Z, Pei Z (2017) Surface grinding of CFRP composites with rotary ultrasonic machining: a mechanistic model on cutting force in the feed direction. Int J Adv Manuf Technol 92(1–4):1217–1229. https://doi.org/10.1007/s00170-017-0149-9
20. Wang H, Cong W, Ning F, Hu Y (2018) A study on the effects of machining variables in surface grinding of CFRP composites using rotary ultrasonic machining. Int J Adv Manuf Technol 95(9–12):3651–3663. https://doi.org/10.1007/s00170-017-1468-6
21. Wang Y, Lin B, Zhang X (2014) Research on the system matching model in ultrasonic vibration-assisted grinding. Int J Adv Manuf Technol 70(1):449–458. https://doi.org/10.1007/s00170-013-5269-2
22. Yuan S, Fan H, Amin M, Zhang C, Guo M (2016) A cutting force prediction dynamic model for side milling of ceramic matrix composites C/SiC based on rotary ultrasonic machining. Int J Adv Manuf Technol 86(1–4):37–48. https://doi.org/10.1007/s00170-015-8099-6
23. Yuan S, Zhang C, Amin M, Fan H, Liu M (2015) Development of a cutting force prediction model based on brittle fracture for carbon fiber reinforced polymers for rotary ultrasonic drilling. Int J Adv Manuf Technol 81(5–8):1223–1231. https://doi.org/10.1007/s00170-015-7269-x
24. Wang Y, Sarin VK, Lin B, Li H, Gillard S (2016) Feasibility study of the ultrasonic vibration filing of carbon fiber reinforced silicon carbide composites. Int J Mach Tools Manuf 101:10–17. https://doi.org/10.1016/j.ijmachtools.2015.11.003
25. Cong WL, Pei ZJ, Sun X, Zhang CL (2014) Rotary ultrasonic machining of cfrp: a mechanistic predictive model for cutting force. Ultra 54(2):663–675. https://doi.org/10.1016/j.ultras.2013.09.005
26. Li P, Zhang W (2014) Experiment based cutting force model for high speed milling of aluminium based composite. Mater Res Innov 18(sup5):S5-35–S35-38. https://doi.org/10.1179/1432891714Z.000000000909
27. Ojo S, Ismail SO, Paggi M, Dhakal H (2017) A new critical thrust force model for delamination of composite laminates: analytical approach using first-order shear deformation theory
28. Cao X, Lin B, Wang Y, Wang S (2014) Influence of diamond wheel grinding process on surface micro-topography and properties of SiO2/SiO2 composite. Appl Surf Sci 292:181–189. https://doi.org/10.1016/j.apsusc.2013.11.109
29. Li Z, Ding W, Liu C, Su H (2018) Grinding performance and surface integrity of particulate-reinforced titanium matrix composites in creep-feed grinding. Int J Adv Manuf Technol 94(9):3917–3928. https://doi.org/10.1007/s00170-017-1159-3
30. Liu C, Ding W, Yu T, Yang C (2018) Materials removal mechanism in high-speed grinding of particulate reinforced titanium matrix composites. Precis Eng 51:68–77. https://doi.org/10.1016/j.precisioneng.2017.07.012